

## MESOSCOPIC NUMERICAL MODEL TO SIMULATE DEGRADATION AND ULTIMATE LOAD CARRYING CAPACITY IN REINFORCED CONCRETE STRUCTURES AFFECTED BY CORROSION

Pablo J. Sánchez<sup>a,c</sup>, Alfredo E. Huespe<sup>a</sup>, Javier Oliver<sup>b</sup> and Sebastián Toro<sup>c</sup>

<sup>a</sup>International Center for Computational Methods in Engineering (CIMEC), Güemes 3450 PTLC, 3000 Santa Fe, Argentina, [psanchez@intec.unl.edu.ar](mailto:psanchez@intec.unl.edu.ar), <http://www.cimec.org.ar>

<sup>b</sup>Polytechnical University of Catalonia (UPC), Campus Nord, Modul C-I, Gran Capitán s/n, 08034 Barcelona, Spain, [xavier.oliver@upc.es](mailto:xavier.oliver@upc.es), <http://www.upc.edu/es>

<sup>c</sup>GIMNI, National Technological University (UTN-FRSF), Lavaise 610, 3000 Santa Fe, Argentina, [storo@frsf.utn.edu.ar](mailto:storo@frsf.utn.edu.ar), <http://www.frsf.utn.edu.ar>

**Keywords:** reinforced concrete structures, corrosion, ultimate load carrying capacity, finite elements with embedded strong discontinuities, loss of steel-concrete adherence, contact elements.

**Abstract.** In this research work, a finite element strategy specially devised to simulate the structural degradation of corroded reinforced concrete members is presented. The proposed model is able to reproduce many of the mechanical effects induced by corrosion processes in the embedded steel bars and, mainly, their influences on the structural ultimate load carrying capacity predictions. For these purposes, two different and coupled mesoscopic problems are considered. This mechanical model can be used to simulate *generalized* or *localized* reinforcement corrosion. Each component of the Reinforced Concrete (RC) structure is modeled by means of a suitable finite element (FE) formulation. For the concrete, a cohesive model based on the *Continuum Strong Discontinuity Approach (CSDA)* is used. The steel reinforcement bars are simulated by means of an elasto-plastic model. The steel-concrete interface is simulated using contact-friction elements with the friction degradation as a function of the depth of corrosion attack. Experimental and previous numerical solutions are used to compare and validate the proposed models.

## 1 INTRODUCTION

Reinforced concrete structures (or simply RC structures) have been widely used across the world due to many technical and constructive advantages. However, several degradation mechanisms affect its durability and the long-term structural reliability. In this context, the corrosion of the embedded reinforcement steel bars is identified as one of the most critical phenomenon influencing the *RC service life*. The problem must be carefully analyzed because it could cause premature deterioration and, sometimes, the necessity of costly repairs, strengthening, replacement or even the demolition of existing structures (Cairns and Millard, 1999).

The economic importance and the technological consequences of this problem have motivated, in the last years, numerous research projects. Thus, they can be mentioned many experimental works reporting the unfavorable corrosion effects on RC elements, see for example Rodriguez et al. (1994, 1995, 1996); Okada et al. (1988); Uomoto and Misra (1988); Tachibana et al. (1990); Cabrera and Ghoddoussi (1992); Almusallam et al. (1996); Al-Sulaimani et al. (1990); Huang and Yang (1997), and also analytical studies and numerical models (Bazant, 1979b,a; Bhargava et al., 2006, 2007; Vecchio, 2001; Castellani and Coronelli, 1999; Coronelli and Gambarova, 2004; Fang et al., 2006) addressed to understand this complex degradation process.

Many kinds of problems are involved in the corrosion of RC members. Here, we specially focus in only one of them, the *structural mechanical problem*. In this context, we describe a numerical model suitable to simulate the evolution of the mechanical degradation mechanisms of RC structural elements caused by the reinforcement fiber corrosion. Phenomena such as: (i) expansion of the corroded bars, (ii) crack pattern distribution, (iii) loss of steel-concrete bond adherence, (iv) net area reduction of the steel fiber cross section and (v) the effects of the above mentioned mechanisms on the structural load carrying capacity, can be analyzed as a function of the reinforcement corrosion degree. A key point in our contribution is that the corrosion attack depth on each steel reinforcement bar, denoted as  $X$ , is a priori known input data.

The proposed numerical model can be applied to any RC structure through two successive and coupled mesoscopic mechanical analyzes, as follows:

- *STAGE I*: at the cross section level, we simulate the reinforcement fiber expansion due to the volume increase of the steel bars as a consequence of corrosion product accumulation (see Section 2). Damage distribution and cracking patterns in the concrete is evaluated, which defines the concrete net section contribution.
- *STAGE II*: considering the results of the previous analysis, a second mesoscopic model at the structural level evaluates the mechanical response of the structural member subjected to an external loading system (see Section 3). This evaluation determines the global response and the macroscopic mechanisms of failure.

We call them mesoscopic analysis because, from the numerical point of view, each component of the RC structure (concrete, steel bars and steel-concrete interface) is represented by itself by means of a suitable FE formulation. Besides, in Section 4, a consistent coupling between the two problems in *STAGE I* and *STAGE II*, is presented.

Finally, applications of such strategies to determine limit loads in RC beams, as a function of the corrosion attack depth, are shown. The obtained quantitative structural ultimate load predictions are compared with available experimental and numerical results.

## 2 STAGE I: THE MESOSCOPIC CROSS SECTION MODEL (EXPANSION MODE)

The products derived from the steel bar corrosion reduce the net steel area and accumulate causing volumetric expansion of the bars (see Figure 1-(a)), what induces a high tensile stress state in the surrounding concrete. As a consequence the concrete undergoes a degradation process displaying two common fracture patterns (Capozucca, 1995): (i) inclined cracks and (ii) delamination cracks, as we can observe in Figure 1-(c). In this section, we present a finite element technique that is specially devised to study this phenomenon.

The 2D plane strain mesoscopic model considers three different domains (see Figure 1-(b)): (i) the concrete matrix, (ii) the steel reinforcement bars and (iii) the steel-concrete interface, each of them are characterized by a different constitutive response and FE technology that takes into account the main mechanisms involved in the corrosion process.

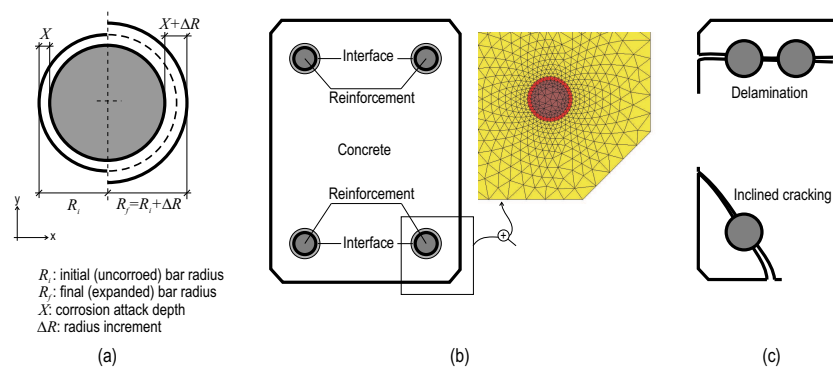


Figure 1: RC structural member cross section. Plane strain mesoscopic 2D model: (a) Corrosion-expansion mechanism. (b) Numerical model idealization. (c) Typical pattern of cracks.

### 2.1 The concrete material

The model adopted for analyzing the concrete matrix is an isotropic continuum damage model regularized by the *Continuum Strong Discontinuity Approach (CSDA)*, as described in Oliver et al. (2002). This technique has been widely discussed in many previous articles. Here we only summarize the main features of this model. Additional details can be obtained elsewhere (Oliver and Huespe, 2004a,b).

The macroscopic discontinuities arising in a quasi-brittle solid, such as fractures, are mathematically described by means of a strong discontinuity kinematics. Let be given a body  $\Omega$  experiencing displacement jumps across the surface  $S$  (see Figure 2). This surface ( $S$ ) divides the body in two disjunct domains  $\Omega^+$  and  $\Omega^-$ . Then the displacement  $\mathbf{u}(\mathbf{x})$  and the compatible strain field tensor  $\boldsymbol{\varepsilon}(\mathbf{x})$ , in  $\Omega$ , can be written as:

$$\mathbf{u}(\mathbf{x}) = \underbrace{\bar{\mathbf{u}}(\mathbf{x})}_{\text{continuous}} + \underbrace{H_S(\mathbf{x}) \llbracket \mathbf{u} \rrbracket(\mathbf{x})}_{\text{discontinuous}} \quad ; \quad H_S(\mathbf{x}) = \begin{cases} 1 & \forall \mathbf{x} \in \Omega^+ \\ 0 & \forall \mathbf{x} \in \Omega^- \end{cases} \quad (1)$$

$$\boldsymbol{\varepsilon}(\mathbf{x}) = \nabla^{\text{sym}} \mathbf{u}(\mathbf{x}) = \underbrace{\bar{\boldsymbol{\varepsilon}}(\mathbf{x})}_{\text{regular}} + \underbrace{\delta_S(\mathbf{x}) (\llbracket \mathbf{u} \rrbracket \otimes \mathbf{n})^{\text{sym}}}_{\text{singular}} \quad (2)$$

where  $\bar{\mathbf{u}}(\mathbf{x})$  is a  $C^0$  continuous function in  $\Omega$ ,  $\llbracket \mathbf{u} \rrbracket(\mathbf{x})$  represents the displacement jump across the surface  $S$  and  $H_S(\mathbf{x})$  is the Heaviside's step function. Note that the strain field shows a singular term, the second one in equation (2), given by the Dirac's delta distribution  $\delta_S(\mathbf{x})$ .

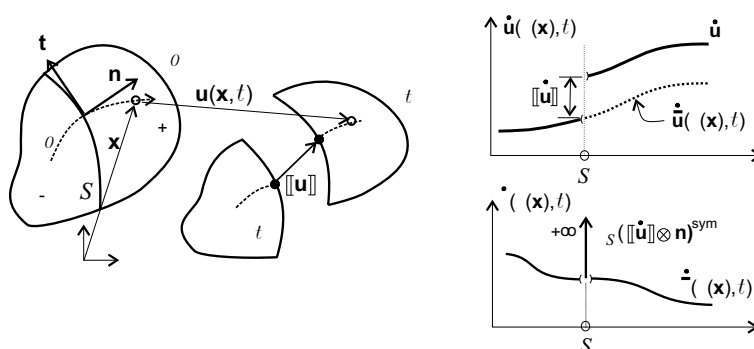


Figure 2: Strong discontinuity kinematics.

Elastic stress-strain relationship

$$\boldsymbol{\sigma} = \frac{q(r)}{r} \mathbf{C}^e : \boldsymbol{\varepsilon} = [1 - d(r)] \overbrace{\mathbf{C}^e : \boldsymbol{\varepsilon}}^{\bar{\boldsymbol{\sigma}}} \quad (3)$$

$$\mathbf{C}^e = \lambda (\mathbb{I} \otimes \mathbb{I}) + 2\mu \mathbb{I} \quad (\text{Isotropic elastic tensor}) \quad (4)$$

$$\mathbb{I} = \delta_{ij} (\mathbf{e}_i \otimes \mathbf{e}_j); \quad \mathbb{I} = \frac{1}{2} (\delta_{ik}\delta_{jl} + \delta_{il}\delta_{jk}) (\mathbf{e}_i \otimes \mathbf{e}_j \otimes \mathbf{e}_k \otimes \mathbf{e}_l) \quad (5)$$

Damage criterion

$$\phi(\boldsymbol{\sigma}, q) = \tau_\sigma - q \leq 0 \quad (6)$$

$$\tau_\sigma = \chi \sqrt{\boldsymbol{\sigma} : (\mathbf{C}^e)^{-1} : \boldsymbol{\sigma}} = \chi [1 - d(r)] \sqrt{\bar{\boldsymbol{\sigma}} : (\mathbf{C}^e)^{-1} : \bar{\boldsymbol{\sigma}}} \quad (7)$$

$$\chi = \frac{\sum_{i=1}^{i=3} \langle \bar{\sigma}_i \rangle}{\sum_{i=1}^{i=3} |\bar{\sigma}_i|} \left[ 1 - \frac{1}{n_\sigma} \right] + \frac{1}{n_\sigma} \quad (8)$$

$$n_\sigma = \frac{\sigma_u^C}{\sigma_u}; \quad \langle \bullet \rangle = \frac{1}{2} \{ \bullet + \| \bullet \| \} \quad (9)$$

$$\bar{\sigma}_i \equiv \text{principal values of } \bar{\boldsymbol{\sigma}} \quad (10)$$

Softening evolution law

$$\dot{r} = \gamma \quad ; \quad r_0 = r|_{t=0} = \frac{\sigma_u}{\sqrt{E}} \quad (11)$$

$$\dot{q} = H(r) \dot{r} \quad ; \quad q_0 = q|_{t=0} = r_0 \quad (12)$$

$$(\gamma \equiv \text{damage consistency parameter}) \quad (13)$$

Loading-unloading complementarity conditions

$$\phi(\boldsymbol{\sigma}, q) \leq 0 \quad ; \quad \gamma \geq 0 \quad ; \quad \gamma \phi(\boldsymbol{\sigma}, q) = 0 \quad (14)$$

Table 1: Continuum damage model for the concrete response simulation.

Concrete can be quite appropriately modelled by means of an isotropic continuum damage models equipped with a regularized strain softening modulus in order to make possible the onset of material instabilities, strain localization and crack propagation. Table (1) defines the adopted material law, where damage in tension and compression is possible, but different ultimate limit stresses are used (Oliver et al., 1990).

There,  $\sigma$  and  $\varepsilon$  represent the stress and strain tensors,  $q$  and  $r$  are internal variables defining the standard scalar damage variable  $d = 1 - (q/r)$ . The elastic material parameters  $E$ ,  $\lambda$  and  $\mu$  are the Young's modulus and the Lamé coefficients. Also we define  $\sigma_u^C$  and  $\sigma_u$  as the compressive and tensile limit strength, respectively.

The compatibility between the strong discontinuity kinematics, eqs. (1)-(2), and the continuum damage material model is taken into account by introducing an intrinsic softening modulus  $\bar{H} = \delta_S H$ , whose value is computed from the classical parameters used in the *Fracture Mechanics* context:  $\bar{H} = f(\sigma_u, G_f, E)$ , where  $G_f$  is the concrete fracture energy. This intrinsic modulus allows to define a bounded stress state in  $S$  through the standard continuum damage model of Table (1), even when the strain tensor has a singular term (see equation (2)).

The vector traction continuity across the discontinuity interface  $S$ , internal equilibrium condition, requires that:

$$t_S = \sigma_S \cdot n = \sigma_{\Omega^+} \cdot n \tag{15}$$

When the strong discontinuity kinematics (1)-(2) is consistently introduced in this continuum setting, a cohesive model (traction separation law)  $t_S = f(\llbracket u \rrbracket)$  is automatically projected onto the interface  $S$  (Oliver, 2000). This traction-separation cohesive model governs the crack opening evolution in the strong discontinuity regime.

The previously discussed model is numerically implemented by using an enhanced finite element technique with embedded strong discontinuities. Basically, this methodology consists of enriching the standard continuous displacement modes adding enhanced discontinuous ones and, consequently, additional degrees of freedom. It makes possible to capture the crack trajectory inside the finite elements irrespective of the size and orientation of them. In particular, so called the Embedded Finite Element Method *E-FEM* (Oliver et al., 2006) has been adopted in the present work, see Figure 3. This strategy permits the condensation of the extra discontinuous modes at elemental level and, therefore, the additional d.o.f. does not enlarge the size of final equation system.

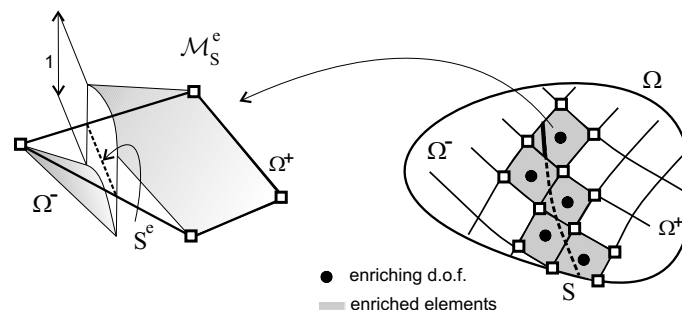


Figure 3: Embedded finite elements with internal enhanced d.o.f. (*E-FEM* technique).

## 2.2 The steel reinforcement bars

Let us assume that the cross section of a typical RC member is contained in the the  $x$ - $y$  plane, as we can observe in the Figure 1-(a). A standard linear elastic (isotropic) constitutive behavior is assumed for the steel bars. The expansion effect, due to the corrosion phenomenon, is considered through a (pseudo) volumetric initial deformation mode  $\varepsilon^0$ . Making use of the standard Voigt's notation for tensors and assuming a plane strain state, the total strain ( $\varepsilon$ ) can be expressed as the superposition of two terms:

$$\varepsilon = \nabla^{sym} \mathbf{u} = \begin{bmatrix} \varepsilon_{xx} \\ \varepsilon_{yy} \\ \gamma_{xy} \\ \varepsilon_{zz} \end{bmatrix} = \begin{bmatrix} \varepsilon_{xx} \\ \varepsilon_{yy} \\ \gamma_{xy} \\ 0 \end{bmatrix} = \overbrace{\begin{bmatrix} \frac{1}{E}(\sigma_{xx} - \nu\sigma_{yy} - \nu\sigma_{zz}) \\ \frac{1}{E}(\sigma_{yy} - \nu\sigma_{zz} - \nu\sigma_{xx}) \\ 2\left(\frac{1+\nu}{E}\right)\sigma_{xy} \\ \frac{1}{E}(\sigma_{zz} - \nu\sigma_{xx} - \nu\sigma_{yy}) \end{bmatrix}}^{\varepsilon^e} + \overbrace{\begin{bmatrix} \mathcal{D} \\ \mathcal{D} \\ 0 \\ 0 \end{bmatrix}}^{\varepsilon^0} \quad (16)$$

where  $\mathcal{D}$  is the value of the dilatational component and  $\varepsilon^e$  the elastic strain tensor. Note that, the dilatational effect is not included in the  $z$  direction.

Taking into account an elastic constitutive relation, the stress field can be computed as:

$$\boldsymbol{\sigma} = \begin{bmatrix} \sigma_{xx} \\ \sigma_{yy} \\ \tau_{xy} \\ \sigma_{zz} \end{bmatrix} = \begin{bmatrix} \lambda + 2\mu & \lambda & 0 & \lambda \\ \lambda & \lambda + 2\mu & 0 & \lambda \\ 0 & 0 & G & 0 \\ \lambda & \lambda & 0 & \lambda + 2\mu \end{bmatrix} \begin{bmatrix} \varepsilon_{xx} - \mathcal{D} \\ \varepsilon_{yy} - \mathcal{D} \\ \gamma_{xy} \\ 0 \end{bmatrix} \quad (17)$$

where  $G$  is the shear modulus.

The dilatation parameter  $\mathcal{D}$  can be estimated as a function of  $X$  (which is an experimentally determined value):

$$\mathcal{D} \approx \frac{R_f^2(X) - R_i^2}{2R_i^2} \quad (18)$$

An approximation for the final bar radius,  $R_f = \hat{R}_f(X)$ , will be given in Section 5.

## 2.3 The steel-concrete interface (contact FE)

The shear stress transference, between the steel reinforcements and the concrete, has a limit value (maximum adherence stress  $\tau_{max}$ ) that depends on several factors: bar diameter, bar surface texture, confining effects, corrosion level, etc. Also, when high expansion values in the steel are reached, separation between both materials, steel and concrete, must be expected. These effects have important consequences in the concrete fracture pattern prediction, what motivates the introduction of special contact finite elements in order to simulate (appropriately) the steel-concrete interface, see Figure 4-(a).

The contact linear triangular element adopted in the present work has been taken from [Oliver et al. \(2007\)](#), where additional details can be obtained. In every contact finite element, a local cartesian system  $\{\boldsymbol{\eta}, \mathbf{t}\}$  is defined, where  $\boldsymbol{\eta}$  is the unit vector normal to the contact surface. The strains are evaluated from the (symmetric) gradient of nodal displacement, as it is done in

standard finite elements. The mechanical response of the contact-friction model is expressed by means of the following constitutive law:

$$\boldsymbol{\sigma} = \Psi(g) \left[ \sigma_{\eta\eta}(\varepsilon_{\eta\eta}) (\boldsymbol{\eta} \otimes \boldsymbol{\eta}) + \tau_{\eta t}(\varepsilon_{\eta t}) [(\boldsymbol{\eta} \otimes \boldsymbol{t}) + (\boldsymbol{t} \otimes \boldsymbol{\eta})] \right] \quad (19)$$

where the scalar step function  $\Psi(g)$ , that takes into account the unilateral contact restriction, is:

$$\Psi(g) = \begin{cases} 1 & ; \text{ if } g < g_0 \\ 0 & ; \text{ if } g \geq g_0 \end{cases} \quad (20)$$

and the gap function,  $g(\varepsilon_{\eta\eta})$ , is computed as:

$$g(\varepsilon_{\eta\eta}) = h^e(1 + \varepsilon_{\eta\eta}) \quad (21)$$

$h^e$  being the length of the finite element in the  $\boldsymbol{\eta}$  direction and  $g_0$  represents an initial gap, which for the present work is assumed  $g_0 = h^e$ .

The normal contact stress,  $\sigma_{\eta\eta}$ , is obtained as a function of the constant strain component  $\varepsilon_{\eta\eta}$  ( $\varepsilon_{\eta\eta} = \boldsymbol{\eta} \cdot \boldsymbol{\varepsilon} \cdot \boldsymbol{\eta}$ ), following a 1D linear elastic law (see Figure 4-(c)). The friction stress component,  $\tau_{\eta t}$ , is determined as a function of the constant shear strain component  $\varepsilon_{\eta t}$  ( $\varepsilon_{\eta t} = \boldsymbol{\eta} \cdot \boldsymbol{\varepsilon} \cdot \boldsymbol{t}$ ) by means of a classical 1D elasto-plastic constitutive model, as detailed in Table (2) (see also Figure 4-(d)). The elasto-plastic model of Table (2) only applies when  $\Psi(g) = 1$ , otherwise no evolution of plastic flow is considered. Thus, the proposed contact-friction model is defined by four parameters: the normal stiffness ( $K_{\eta\eta}$ ), the shear stiffness ( $K_{\eta t}$ ), the maximum stress adherence ( $\tau_{max}$ ) and the hardening/softening shear modulus ( $\bar{K}$ ).

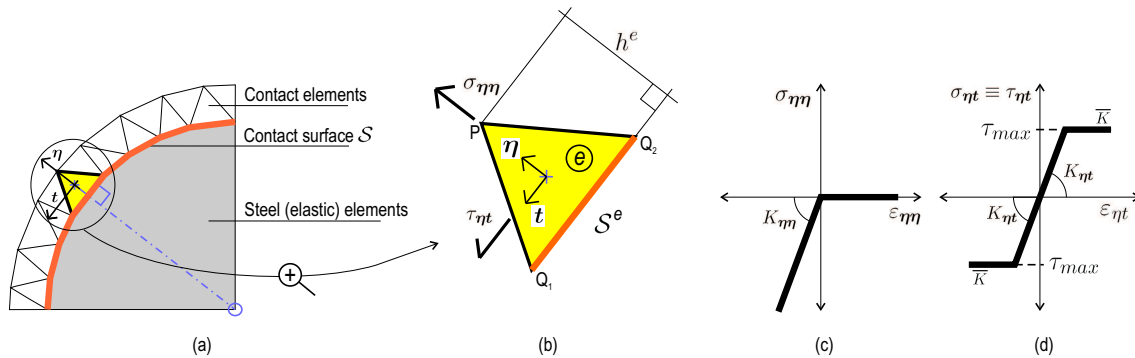


Figure 4: Contact finite element at the interface: (a) Representative scheme. (b) Typical contact finite element. (c) Scheme of the constitutive law for the contact normal stress ( $\sigma_{\eta\eta}$ ). (d) Scheme of the constitutive law for the friction shear stress ( $\tau_{\eta t}$ ).

### 3 STAGE II: THE MESOSCOPIC STRUCTURAL MODEL (FLEXURE)

Now we introduce a 2D mesoscopic model for the quantitative prediction of residual load carrying capacity of corroded RC members, where each component of the structure (concrete, steel and steel-concrete interface) is independently represented. An idealized scheme of the adopted discrete model, applied in particular to a RC beam, can be observed in Figure 5.

The present (plane stress) mesoscopic strategy shares many features with the previous (plane strain) mesoscopic model of the Section (2). In fact, for the concrete we use, again, the *CSDA* with identical enhanced finite elements technology, isotropic (tension-compression) continuum

<u>Incremental elastic stress-strain relationship</u>	
$\dot{\tau}_{\eta t} = K_{\eta t} (\dot{\varepsilon}_{\eta t} - \dot{\varepsilon}_{\eta t}^p)$	(22)
<u>Yield condition</u>	
$\phi(\tau_{\eta t}, \alpha) =  \tau_{\eta t}  - (\tau_{max} + \bar{K}\alpha) \leq 0$	(23)
<u>Flow rule and hardening/softening evolution law</u>	
$\dot{\varepsilon}_{\eta t}^p = \gamma \text{sign}(\tau_{\eta t})$	(24)
$\dot{\alpha} = \gamma$	(25)
$(\gamma \equiv \text{plastic multiplier})$ $(\alpha \equiv \text{accumulated equivalent plastic strain})$	
<u>Loading-unloading complementarity conditions</u>	
$\phi(\tau_{\eta t}, \alpha) \leq 0 \quad ; \quad \gamma \geq 0 \quad ; \quad \gamma \phi(\tau_{\eta t}, \alpha) = 0$	(26)

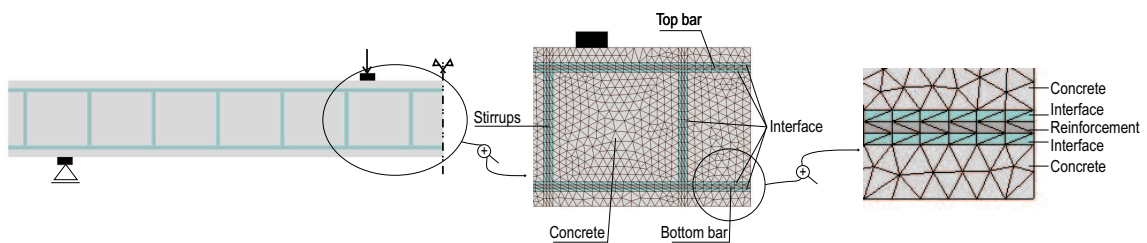
Table 2: Basic equations for the 1D elasto-plastic friction model ( $\tau_{\eta t}$  shear stress).

Figure 5: Plane stress mesoscopic 2D model.

damage model and crack propagation scheme, as it was described in sub-Section 2.1. Also, the same contact finite elements technique, presented in sub-Section 2.3, is used here to simulate the interface effects.

The mechanical behavior of the longitudinal reinforcement steel bars is simulated with an elasto-plastic model, which is briefly discussed next.

### 3.1 Elasto-plastic model for the reinforcement bars

The steel bar response is characterized by a 2D finite element model. Each triangular FE has associated a local normalized cartesian basis  $\{\boldsymbol{\eta}, \boldsymbol{t}\}$ , where the vector  $\boldsymbol{\eta}$  is computed such that it is orthogonal to the longitudinal bar axis, see Figure 6-(a). The mechanical behavior of reinforcements reproduces a 1D standard elasto-plastic model in the  $\sigma_{tt}$  normal stress component, while the remaining stress tensor components behave elastically. Also we have assumed a Poisson relation:  $\nu = 0$ .

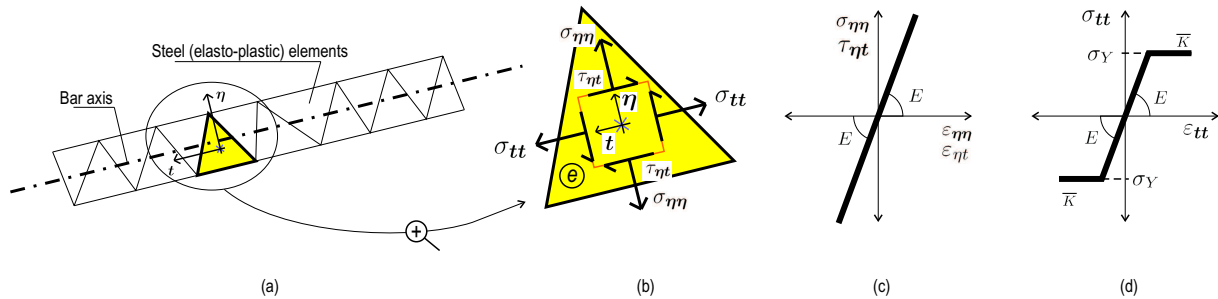


Figure 6: Elasto-plastic reinforcement element: (a) Representative scheme. (b) Typical steel element. (c) Scheme of the constitutive law for  $\sigma_{\eta\eta}$  and  $\tau_{\eta t}$  stresses. (d) Scheme of the constitutive law for  $\sigma_{tt}$  stress.

Taking into account the previous considerations, the stress tensor is given by:

$$\boldsymbol{\sigma} = \sigma_{\eta\eta} (\boldsymbol{\eta} \otimes \boldsymbol{\eta}) + \tau_{\eta t} [(\boldsymbol{\eta} \otimes \boldsymbol{t}) + (\boldsymbol{t} \otimes \boldsymbol{\eta})] + \sigma_{tt} (\boldsymbol{t} \otimes \boldsymbol{t}) \quad (27)$$

where  $\sigma_{\eta\eta} = E \varepsilon_{\eta\eta}$ ,  $\tau_{\eta t} = \tau_{t\eta} = G \varepsilon_{\eta t}$  ( $G$  being the shear elastic modulus) see Figure 6-(c), and  $\sigma_{tt}$  is given by the standard 1D plasticity model, see Figure 6-(d).

## 4 COUPLING STRATEGY: CROSS SECTION MODEL - STRUCTURAL MODEL

Figure 7 shows a simple scheme of the strategy adopted in this contribution to couple the two models presented in the previous sections, i.e., the cross section analysis (*STAGE I*) and the structural member analysis (*STAGE II*).

As we can observe in the figure, for an arbitrary control cross section, we transfer from one domain of analysis to the other, the average value of the damage variable “ $d$ ” across horizontal slices. This projection is consistent because both analysis use the same continuum isotropic damage model for simulating the concrete domain. Thus, the final degradation state of concrete, induced by the steel bar volumetric deformation process, is considered to be the initial damage condition for the subsequent structural analysis.

In this paper we are specially interested in the simulation of generalized corrosion phenomenon, then a unique control cross section is considered, for each RC member, and the mapping of the damage variable is applied homogeneously in the length of this structural member, see Figure 7. However, the same coupling strategy could be easily adapted to model localized corrosion.

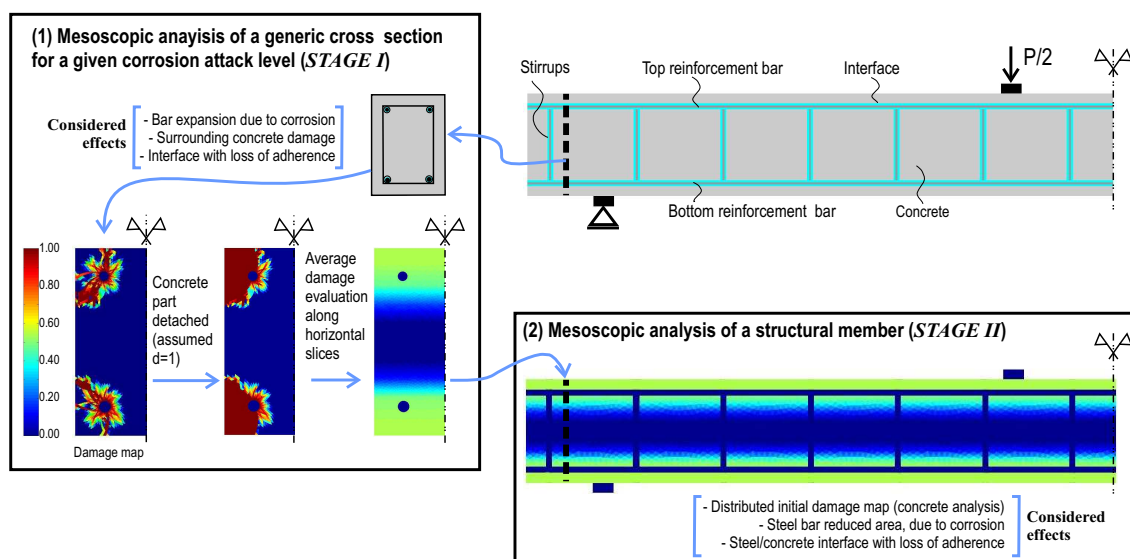


Figure 7: Coupling strategy between the cross section analysis and the structural member analysis.

## 5 APPLICATIONS TO CORRODED RC BEAM TESTS

In this section, a set of numerical simulations are addressed in order to validate the numerical performance of the described FE formulations. Two types of RC beams have been analyzed: Beam type 11 and 31 (additional indices will be added to indicate different corrosion levels for each beam). The geometry and boundary conditions of the problems are shown in Figure 8. Table 3 presents additional information.

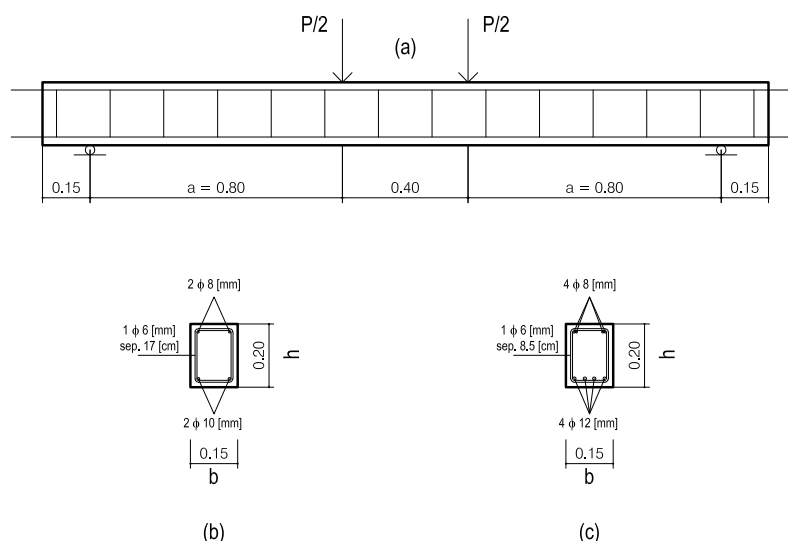


Figure 8: RC Beams: (a) Dimensions and boundary conditions. (b) Cross section scheme for Beam Type 11. (c) Cross section scheme for Beam Type 31.

For these specimens, experimental results are available, see Rodriguez et al. [Rodriguez et al. \(1995, 1996\)](#). In these works a process of accelerated corrosion was induced. Table 4 shows some experimental measurements of the attack depth  $X$ , for different levels of corrosion and types of reinforcement.

Linear triangular finite elements have been adopted for all the tests. In particular, enhanced strong discontinuity triangular elements are used for the concrete material, see sub-Section 2.1.

(1) Beam type	(2) Dimensions $l \times b \times h$ [m]	(3) Top bars: number and diameter [mm]	(4) Bottom bars: number and diameter [mm]	(5) Stirrups: diameter and spacing [mm]	(6) Concrete strength: $\sigma_u^C$ [MPa]	(7) Steel yield stress: $\sigma_Y$ [MPa]
11	$2.00 \times 0.15 \times 0.20$	$2 \phi 8$	$2 \phi 10$	$\phi 6/170$	50 – 34	575
31	$2.00 \times 0.15 \times 0.20$	$4 \phi 8$	$4 \phi 12$	$\phi 6/85$	49 – 37	575

Table 3: RC beams. Material description

(1) Beam denomination	(2) Bottom bars attack: $X_B$ [mm]	(3) Top bars attack: $X_T$ [mm]	(4) Stirrup attack: $X_S$ [mm]	(5) $\tau_{max}$ [MPa]
11 – 1	—	—	—	6.86
11 – 4	0.45	0.52	0.39	4.10
11 – 5	0.36	0.26	0.37	4.13
11 – 6	0.70	0.48	0.66	4.04
31 – 1	—	—	—	7.82
31 – 3	0.30	0.20	0.35	5.12
31 – 4	0.48	0.26	0.50	5.06

Table 4: Experimental corrosion attack measures and residual adherence stress  $\tau_{max}$ . Beams Type 11 and 31

Each numerical problem is solved by imposing an arc-length control strategy. In the plane strain expansion tests, the control is applied over the dilatation variable  $\mathcal{D}$ . For the bending examples, we control the vertical displacement of the beam central point. A very robust constitutive integration scheme is adopted, namely the *Impl-Ex* method (Oliver et al., 2007). Also, in order to optimize the computational resources, we have taken advantage of as many symmetry conditions as possible.

The material parameter characterization considers the following aspects (in this sense we follow very close the guidelines reported in Coronelli and Gambarova (2004)):

- The concrete compressive limit strength,  $\sigma_u^C$ , is given in Table 3, column 6 (the first figure corresponds to the concrete used in the not corroded beams and the second one to the contaminated concrete mixture). The ultimate concrete tensile stress,  $\sigma_u$ , is assumed as:  $\sigma_u = 0.10 \sigma_u^C$ . Other material properties for the concrete, as for example Young's modulus, Poisson's ratio, fracture energy and softening modulus, have been adopted by setting standard values.
- The contact model depends on the ultimate adherence stress  $\tau_{max}(X)$ . Column 5 of Table 4 (see also Rodriguez et al. (1994)) provides a reasonable estimation for the bond-slip model, as a function of the corrosion attack depth.
- The dilatation coefficient  $\mathcal{D}$ , used in the mesoscopic plane strain model, is computed from equation (18). Following Molina et al. (1993) and Coronelli and Gambarova (2004) we adopt the approximation:  $R_f = R_i + X$ , which is based on the incompressibility assumption of the corrosion products. For each solved case, the  $X$  value is adopted from Table 4, columns 2-4.
- Finally, the steel yield stress ( $\sigma_Y$ ) is reported in Table 3, column 7. The reinforcement cross section reduction, due to corrosion, is computed assuming an effective bar radius

$R_{eff} = R_i - X$ . Note that both characterizations apply only to the structural member analysis.

### 5.1 Numerical results: the mesoscopic cross section model

The sequence of Figures 9-11 shows, for the beam type 11 at the final stage of analysis, the iso-displacement contour lines, the FE mesh in the deformed configuration and the damage distribution in the cross section. A complete degradation of the surrounding concrete is observed for the applied expansions level. It can be noted that the main local failure mechanism is an inclined crack pattern.

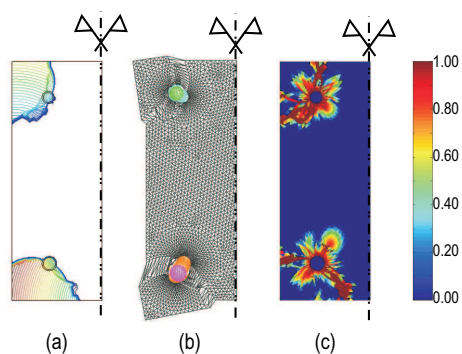


Figure 9: Plane strain expansion analysis. Beam type 11-4: (a) Iso-displacement contour lines (pattern of cracks). (b) Deformed configuration. (c) Damage map.

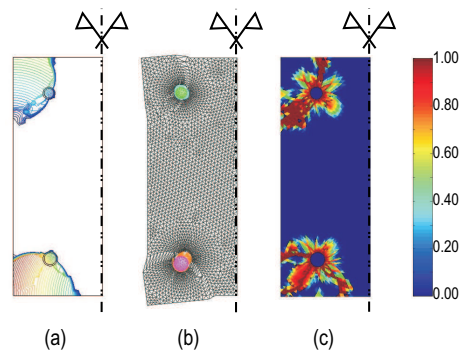


Figure 10: Plane strain expansion analysis. Beam type 11-5: (a) Iso-displacement contour lines (pattern of cracks). (b) Deformed configuration. (c) Damage map.

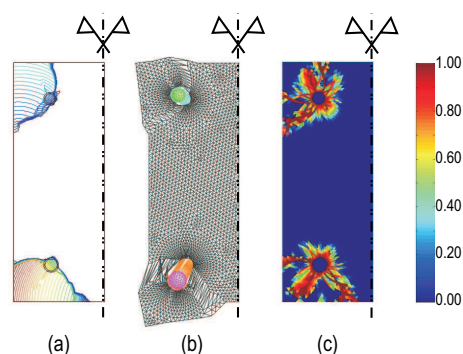


Figure 11: Plane strain expansion analysis. Beam type 11-6: (a) Iso-displacement contour lines (pattern of cracks). (b) Deformed configuration. (c) Damage map.

Figures 12-13 show, for the beam type 31 and at the final stage of analysis, the iso-displacement contour lines, the deformed configuration and the damage map. A complete concrete degradation around the bars is observed. In this case, the local failure mechanism consists of delamination, between adjacent bars, and inclined cracking for the extreme steel fiber.

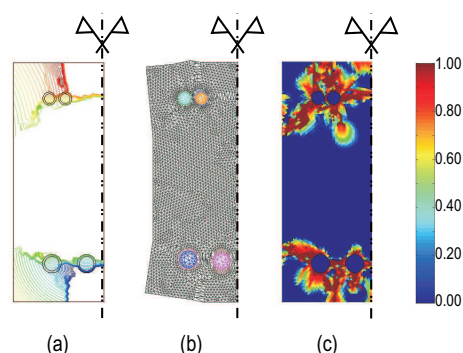


Figure 12: Plane strain expansion analysis. Beam type 31-3: (a) Iso-displacement contour lines (pattern of cracks). (b) Deformed configuration. (c) Damage map.

In general, at the cross section level and from a qualitative point of view, it can be observed that the proposed numerical scheme captures physically admissible failure mechanisms.

## 5.2 Numerical results: the mesoscopic structural model

Figures 14-15 depict the obtained damage distribution, the trajectory of macro cracks as iso-displacement contour lines (in the x-direction) and the contour fill of the axial  $\sigma_{zz}$  stress, for two of the beams type 11 (the not corroded case 11-1 and the corroded one 11-4, see Table 4).

The same analysis of the obtained numerical results can be applied to beam type 31, see Figures 16-17.

In all the studied cases a vertical macro crack, located in the central zone of the beam, has been identified as the fundamental macroscopic failure mechanism determining the limit load. It is characterized by a mode I of fracture, which is the typical ones for those cases of slightly RC beams.

In the Figures 18-24, we show the vertical load vs. the mid span vertical displacement curves for the beam type 11. A good agreement with the experimental data (Rodríguez et al., 1995) and numerical results of Coronelli and Gambarova (2004), has been obtained.

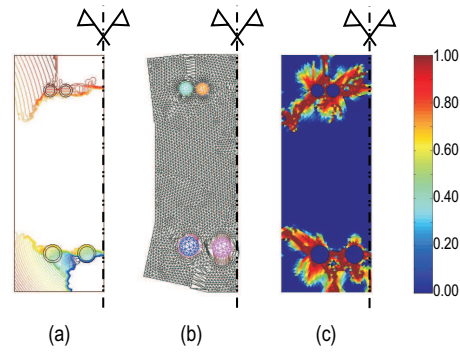


Figure 13: Plane strain expansion analysis. Beam type 31-4: (a) Iso-displacement contour lines (pattern of cracks). (b) Deformed configuration. (c) Damage map.

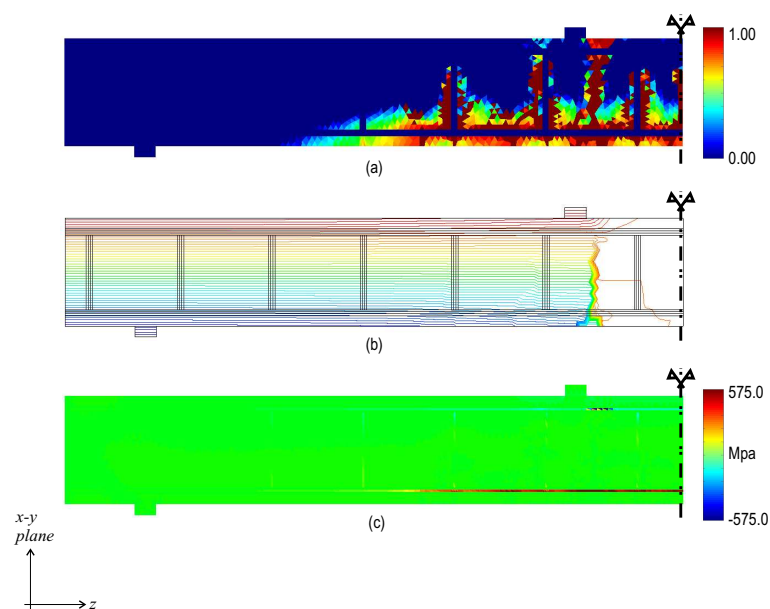


Figure 14: Qualitative results for plane stress mesoscopic model. Beam type 11-1 (not corroded): (a) Contour fill of damage. (b) Iso-displacement contour lines in x-direction. (c) Contour fill of  $\sigma_{zz}$ .

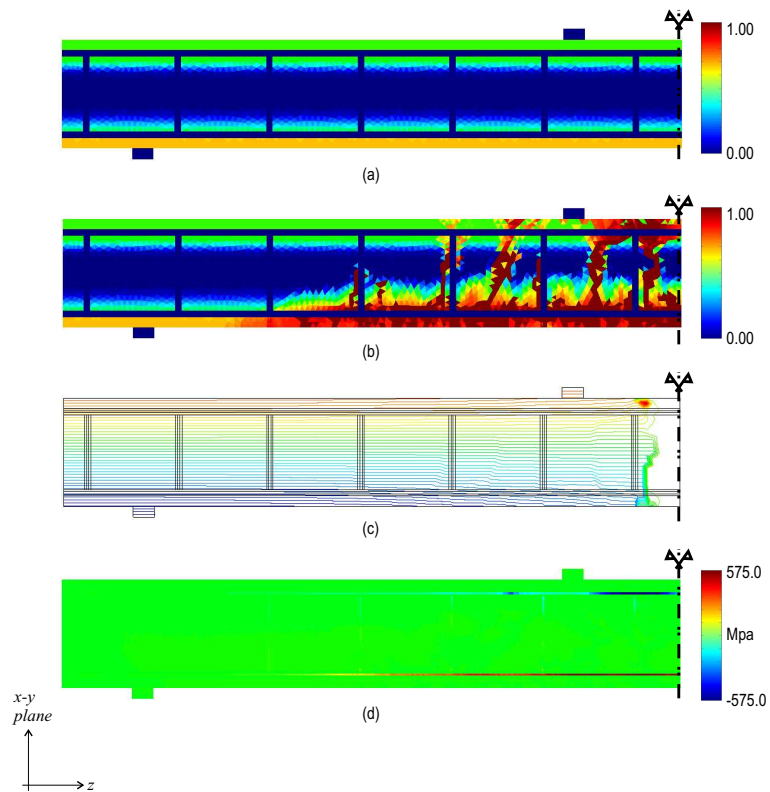


Figure 15: Qualitative results for plane stress mesoscopic model. Beam type 11-4: (a) Initial damage condition. (b) Final contour fill of damage. (c) Iso-displacement contour lines in x-direction. (d) Contour fill of  $\sigma_{zz}$ .

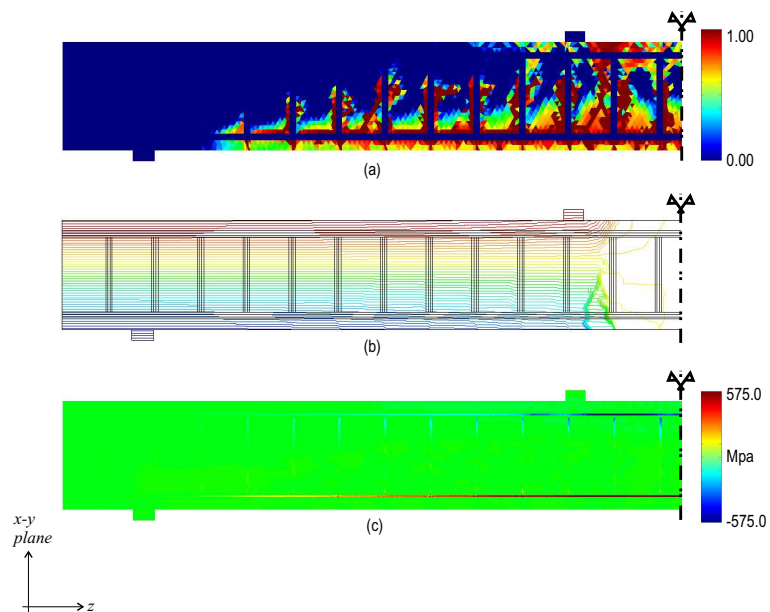


Figure 16: Qualitative results for plane stress mesoscopic model. Beam type 31-1 (not corroded): (a) Contour fill of damage. (b) Iso-displacement contour lines in x-direction. (c) Contour fill of  $\sigma_{zz}$ .

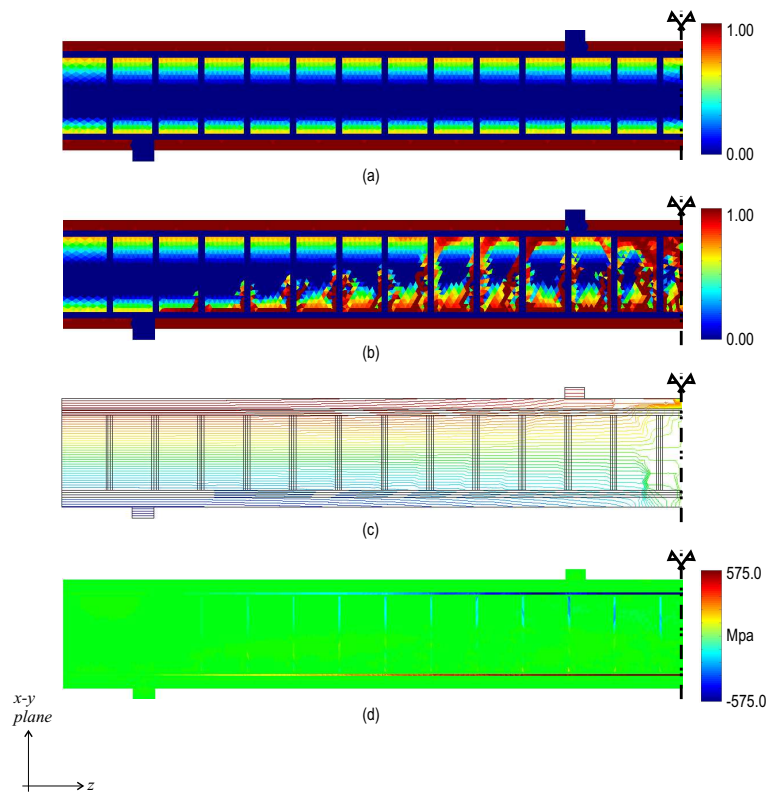


Figure 17: Qualitative results for plane stress mesoscopic model. Beam type 31-3: (a) Initial damage condition. (b) Final contour fill of damage. (c) Iso-displacement contour lines in x-direction. (d) Contour fill of  $\sigma_{zz}$ .

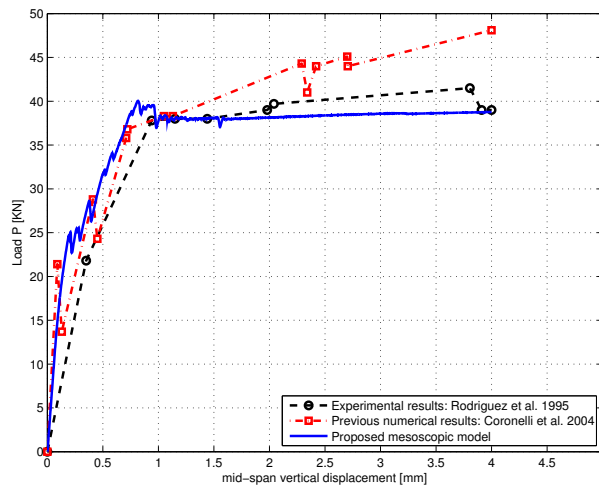


Figure 18: Load vs. displacement structural response. Beam type 11-1

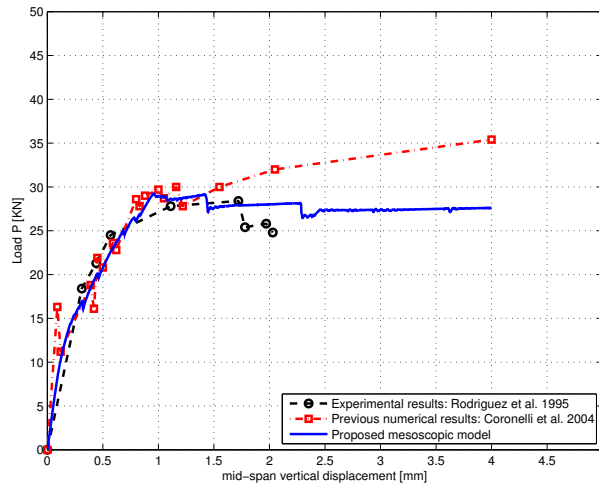


Figure 19: Load vs. displacement structural response. Beam type 11-4

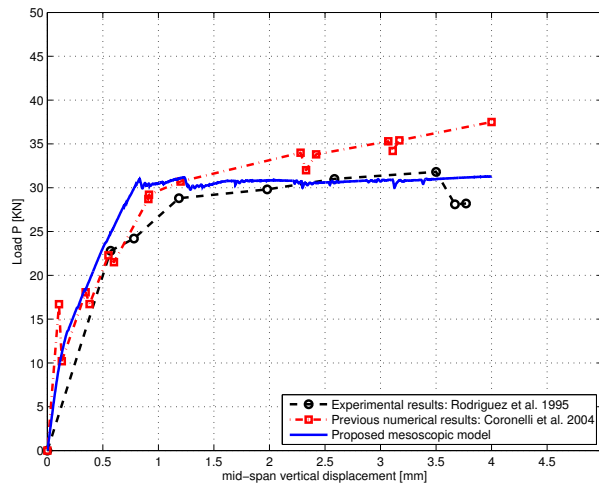


Figure 20: Load vs. displacement structural response. Beam type 11-5

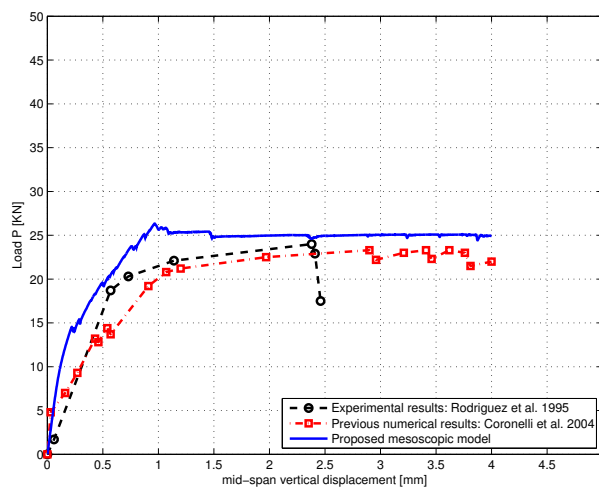


Figure 21: Load vs. displacement structural response. Beam type 11-6

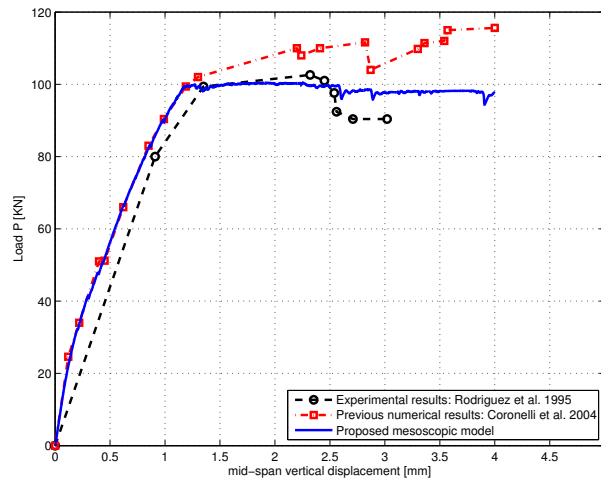


Figure 22: Load vs. displacement structural response. Beam type 31-1

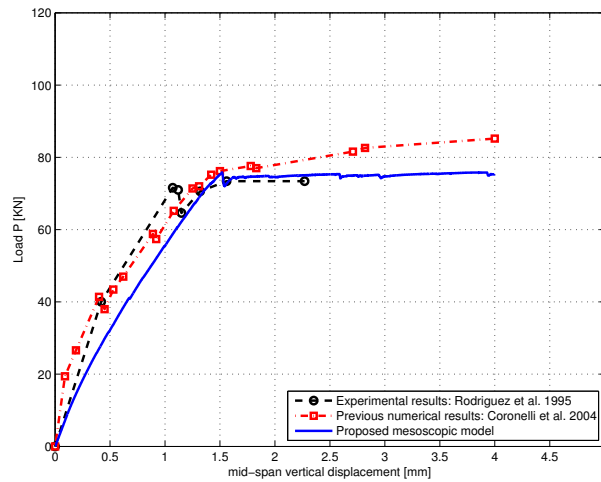


Figure 23: Load vs. displacement structural response. Beam type 31-3

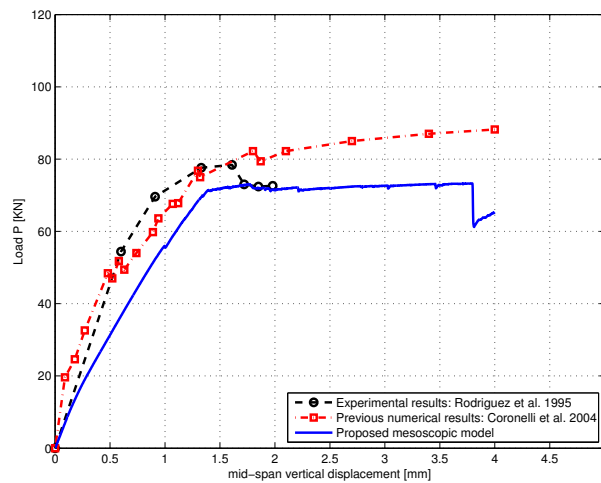


Figure 24: Load vs. displacement structural response. Beam type 31-4

## 6 CONCLUSIONS

In this contribution, we have presented applications of the *CSDA* to solve RC structural beams undergoing a generalized corrosion phenomenon. As a novel contribution, two different mesoscopic size-scale model have been developed. A coupling strategy between them has also proposed.

Contact finite elements were introduced in these formulations in order to improve the simulation of the steel-concrete interface effects. Following the proposed methodology, the most relevant corrosion mechanisms can be simulated, as for example: expansion of steel bars, damage/cracking/spalling in the concrete, yielding in the reinforcement, bond stress degradation at the interface and steel section reduction. In summary, the proposed model represents a viable technique to analyze deteriorated RC members.

The mesoscopic (plane strain) cross section model captures, adequately, the experimental patterns of cracks. Inclined cracking or delamination modes have been obtained, depending on the location and separation of reinforcement bars. The proposed model can be applied to more sophisticated RC cross sections geometrical designs to obtain a qualitative idea of the deterioration mechanisms induced by the expansion-corrosion process.

The mesoscopic (plane stress) structural model captures physically admissible concrete degradation patterns. In all the analyzed cases a typical mode I of fracture, characterizing the final macroscopic failure mechanism, has been observed. The sensitivity of the limits load evaluations with the reinforcement corrosion level as been acceptably computed.

## ACKNOWLEDGEMENTS

Financial support from the Spanish Ministry of Science and Technology trough grant BIA2005-09250-C03-03 and from ANPCyT of Argentina through grant PICT-2005- 34273, are gratefully acknowledged.

## REFERENCES

- Al-Sulaimani G., Kaleemullah M., Basumbul I., and Rasheeduzzafar. Influence of corrosion and cracking on bond behavior and strength of reinforced concrete members. *ACI Struct. J.*, 87(2):220–231, 1990.
- Almusallam A., Al-Gahtani A., Aziz A., and Rasheeduzzafar. Effect of reinforcement corrosion on bond strength. *Constr. Build. Mater.*, 10(2):123–129, 1996.
- Bazant Z. Physical model for steel corrosion in concrete sea structures - applications. *J. Struct. Div.*, pages 1155–1165, 1979a.
- Bazant Z. Physical model for steel corrosion in concrete sea structures - theory. *J. Struct. Div.*, pages 1137–1153, 1979b.
- Bhargava K., Ghosh A., Mori Y., and Ramanujam S. Model for cover cracking due to rebar corrosion in rc structures. *Engineering Structures*, 28:1093–1109, 2006.
- Bhargava K., Ghosh A., Mori Y., and Ramanujam S. Corrosion-induced bond strength degradation in reinforced concrete- analytical and empirical models. *Nuclear Engineering and Design*, 237:1140–1157, 2007.
- Cabrera J. and Ghoddoussi P. The effect of reinforcement corrosion on the strength of the steel/concrete bond. In *Proc. Int. Conf. on Bond in Concrete*, pages 10/11–10/24. CEB, Riga, Latvia, 1992.
- Cairns J. and Millard S. Section 13.2: Reinforcement corrosion and its effects on residual

- strength of concrete structures. In M. Forde, editor, *Proc. 8<sup>th</sup> Int. Conf. on Structure Faults and Repair 99*, pages (CD-ROM). Engineering Tech. Press, Edinburgh, U.K., 1999.
- Capozucca R. Damage to reinforced concrete due to reinforcement corrosion. *Construction and Building Materials*, 9(5):295–303, 1995.
- Castellani A. and Coronelli D. Section 13.7: Beams with corroded reinforcement: Evaluation of effects of cross section losses and bond deterioration by finite element analysis. In M. Forde, editor, *Proc. 8<sup>th</sup> Int. Conf. on Structure Faults and Repair 99*, pages (CD-ROM). Engineering Tech. Press, Edinburgh, U.K., 1999.
- Coronelli D. and Gambarova P. Structural assessment of corroded reinforced concrete beams: modeling guidelines. *J. Struct. Eng. ASCE*, 130(8):1214–1224, 2004.
- Fang C., Lundgren K., Plos M., and Gylltoft K. Bond behaviour of corroded reinforcing steel bars in concrete. *Cement and Concrete Research*, 36:1931–1938, 2006.
- Huang R. and Yang C. Condition assessment of reinforced concrete beams relative to reinforcement corrosion. *Cement & Concrete Composite*, 19:131–137, 1997.
- Molina F., Alonso C., and Andrade C. Cover cracking as a function of rebar corrosion. ii: Numerical model. *Mater. Struct.*, 26:532–548, 1993.
- Okada K., Kobayashi K., and Miyagawa T. Influence of longitudinal cracking due to reinforcement corrosion on characteristics of reinforced concrete members. *ACI Struct. J.*, 85(2):134–140, 1988.
- Oliver J. On the discrete constitutive models induced by strong discontinuity kinematics and continuum constitutive equations. *Int. J. Solids Struct.*, 37:7207–7229, 2000.
- Oliver J., Cervera M., Oller S., and Lubliner J. Isotropic damage models and smeared crack analysis of concrete. In N.B. et al. editor, *SCI-C Computer Aided Analysis and design of concrete Structures*, pages 945–957. Pineridge Press, Swansea, 1990.
- Oliver J. and Huespe A. Theoretical and computational issues in modelling material failure in strong discontinuity scenarios. *Comput. Meth. App. Mech. Eng.*, 193:2987–3014, 2004a.
- Oliver J., Huespe A., and Sánchez P. A comparative study on finite elements for capturing strong discontinuities: e-fem vs x-fem. *Comput. Methods Appl. Mech. Engrg.*, 195(37-40):4732–4752, 2006.
- Oliver J. and Huespe A.E. Continuum approach to material failure in strong discontinuity settings. *Comp. Meth. Appl. Mech. in Engrg.*, 193:3195–3220, 2004b.
- Oliver J., Huespe A.E., and Cante J. An implicit/explicit integration scheme to increase computability of non-linear material and contact/friction problems. *Comp. Meth. Appl. Mech. in Engrg.*, In press, Corrected proof. Available on line 8 December, 2007.
- Oliver J., Huespe A.E., Pulido M.D.G., and Chaves E. From continuum mechanics to fracture mechanics: the strong discontinuity approach. *Engineering Fracture Mechanics*, 69:113–136, 2002.
- Rodriguez J., Ortega L., and Casal J. Load carrying capacity of concrete structures with corroded reinforcement. In M. Forde, editor, *4<sup>th</sup> Int. Conf. on Structure Faults and Repair*, pages 189–199. Engineering Tech. Press, Edinburgh, U.K., 1995.
- Rodriguez J., Ortega L., and Garcia A. Corrosion of reinforcing bars and service life of r/c structures: Corrosion and bond deterioration. In *Proc. Int. Conf. on concrete across Borders*, volume 2. Odense, Denmark, 1994.
- Rodriguez J., Ortega M., Casal J., and Diez M. Assessing structural conditions of concrete structures with corroded reinforcement. In R.D. Dundee Scotland and N. Henderson, editors, *Proc. Int. Conf. on Concrete in the Service of Mankind*, pages 141–150. E&FN Spon, London, 1996.

- Tachibana Y., Kajakawa K.M.Y., and Kawamura M. Mechanical behaviour of rc beams damage by corrosion of reinforcement. In *Proc. 3<sup>dr</sup> International Symposium on Corrosion of Reinforcement in Concrete Construction*, pages 178–187. Wishaw, UK, 1990.
- Uomoto T. and Misra S. Behaviour of concrete beams and columns in marine environments when corrosion of reinforcing bars takes place. *ACI Special Publication*, SP-109:127–145, 1988.
- Vecchio F. Nonlinear finite element analysis of reinforced concrete: At the crossroads? *Struct. Concr.*, 2(4):201–212, 2001.